Iranian Journal of Materials Science and Engineering, Vol. 20, Number 2, June 2023
RESEARCH PAPER

Influence of Friction Stir Processing Parameters on the Mechanical and Corrosion Properties of Al-Cu-Li Alloy

Sandeep Ramasamy Periasamy[1], Vaira Vignesh Ramalingam[1,*], Ajay Vijayakumar[1], HarieHarran Senthilkumaran[1], VyomaTeja Sajja[1], Padmanaban Ramasamy[1], Samuel Ratna Kumar Paul Sureshkumar[2]

* *r_vairavignesh@cb.amrita.edu*

[1] Department of Mechanical Engineering, Amrita School of Engineering, Coimbatore, Amrita Vishwa Vidyapeetham, India
[2] Department of Industrial and Mechanical Engineering, University of Johannesburg, Johannesburg, South Africa

Received: February 2022 **Revised: May 2023** **Accepted: May 2023**
DOI: 10.22068/ijmse.2670

Abstract: *In this work, AA2050 alloy was friction stir processed at various tool rotation speeds and feed rates. The material was subjected to artificial aging to investigate its influence on macrostructure, microstructure, microhardness, and tensile strength of friction stir processed AA2050. In addition, a hot salt corrosion test was done on the test specimens at 130°C for 168 hours. The results indicated that grain refinement and dispersion of secondary phase particles improved the microhardness and strength of friction stir processed specimens. The artificial aging of the friction stir processed specimens improved the ductility by 81.5%. However, the tensile strength of the specimens decreased by 2.8%. The corrosion (mass loss per unit area) of the specimen processed with a single pass at a speed of 600 rpm and feed rate of 60 mm/min decreased by 90% compared to the base material.*

Keywords: *Friction stir processing, Al-Cu-Li alloy, Microstructure, Heat Treatment, Corrosion.*

1. INTRODUCTION

Al-Cu-Li alloy of the 2xxx aluminum alloy series (AA2050, AA2060, AA2198) possesses a high strength-to-weight ratio compared to other alloys and delivers superior fatigue performance. The inherent formation of intermetallic phases through the reaction of Al with the alloying elements Cu and Li accelerates the corrosion rate of the material. This is one of the severe limitations that have to be overcome by Al-Cu-Li alloy to be preferred in the aerospace industry. The phases present in the form of precipitates, dispersoids, and intermetallic phases play an important role in determining the properties of the Al-Cu-Li alloy. The intermetallic phases can be engineered or modified by various processes like surface modifications such as micro-arc oxidation, plasma oxidation, the addition of new alloying elements, heat treatment cycle, and other processing methodologies. However, the intermetallic phases of Al-Cu-Li alloy will not be modified to a greater extent by the above-mentioned processes. Hence, particle dissolution and mechanical fragmentation of intermetallic phases are deemed necessary. Severe plastic deformation processes such as Equal Channel Angular Pressing (ECAP), forging, cryo-forging, and high-pressure torsion process assist mechanical fragmentation of intermetallic phases in AL-Cu-Li alloy. Al-Cu-Li alloy dynamically softens when processed at higher temperature conditions and lower strain rate conditions [1]. Hence, the stress level significantly decreases with an increase in temperature and/or with a decrease in the strain rate of the process. The plastic deformation processes like ECAP increases strength but decrease the ductility of Al-Cu-Li alloys. Research shows that the impact toughness could be increased by increasing the number of ECAP processes. With the decrease in processing temperature, the average grain size decreases. However, the variation of dislocation density shows the opposite trend because of hindered recovery [2]. Cumulatively, reducing grain size and increasing dislocation density improves the mechanical properties (hardness and strength) of the Al-Cu-Li alloys. It was observed that the grains of the cryo-forged Al-Cu-Li alloy are finer at all cycle conditions than room temperature forged alloy. Also, a direct relationship exists between the strain and average grain size [3]. The grain size decreases, then increases, and finally levels off along the radial direction in the Al-Cu-Li alloy subjected to high-pressure torsion. The mechanical properties

[DOI: 10.22068/ijmse.2670]

significantly increase, which is attributable to grain refinement and dislocation strengthening. The (Al_2Cu) precipitates were less thermally stable as compared to the (Al_2CuLi) precipitates [4]. α-Al grains, reduction, and dissolution of both the eutectic phase ($CuAl_2$) and the strengthening precipitates ($CuAl_2$) improved the corrosion resistance of friction stir processed (FSPed) Al-Cu-Li alloys [5-7]. Aging treatment also improves the tensile properties and intergranular corrosion resistance of Al-Cu-Li alloys [8]. The microhardness test reveals that magnesium has a vital role in influencing the microhardness of the specimens, as they diffuse more into aluminum and copper [9]. Friction stir processing (FSP) is one of the solid-state processing techniques [10, 11], which could be effectively utilized to alter the microstructure and hence the properties of Al-Cu-Li alloys. This process has less work stress on the working material, and its reliability is higher than its competitors [12, 13]. Literature reported refined grains and dispersed secondary phases in FSPed Al-Cu-Li alloys. A defect-free zone could be observed in the FSPed specimens processed under low axial forces and at higher welding and tool rotation speeds [14]. Also, brittle to-ductile transformation is observed in Al-Cu-Li alloys when the strain rate lessens and the temperature increases [15, 16]. The dissolution and coarsening sequences of precipitates cause variation in the properties [17, 18]. It is observed that most of the literature work on aluminum alloys focused on strengthening alloys. However, the influence of processing parameters and heat treatment on the properties of FSPed AA2050 alloy is seldom discussed in the open literature. This study concentrates on the microhardness, tensile strength, and corrosion properties of FSPed AA2050. Also, the research focuses on the influence of artificial aging on the microhardness and tensile strength of the FSPed AA2050.

2. EXPERIMENTAL PROCEDURES

2.1. Materials

The composition of the as-received AA2050 alloy (Table 1) indicates the conformity of the received AA2050 alloy to the information provided by The Aluminum Association, Inc. from International Alloy Designations and Chemical Composition Limits for Wrought Aluminum and Wrought Aluminum Alloys [19]. AA2050 alloy plates of the size of 200 × 100 × 5 mm were prepared for FSP trials using wire-cut electric discharge machining (wire EDM).

2.2. Experimental Set Up

FSP trials were performed in a dedicated friction stir welding setup at Amrita Vishwa Vidyapeetham (Coimbatore Campus). The tool was made from high carbon high chromium steel with dimensions shown in Figure 1. The FSP process parameters, namely tool rotation speed, feed rate, and the number of passes were varied as per the experimental plan shown in Table 2. The tool rotation speed and feed rate were controlled using a PID controller. The required speed was set, and the tool pin was slowly plunged until the shoulder touched the workpiece. Then the auto-feed is turned on to complete the FSP trial. The FSPed workpieces were cut along the cross-section to specimens of size 20 × 10 × 5 mm. The cold set specimens were flattened on both sides with the help of a belt grinder. The scratches were removed by polishing with 400, 600, 800, and 1000 grade emery papers. Subsequently, the specimens were polished in a disc polisher with velvet cloth wetted with alumina suspension in distilled water to mirror the finish. The specimens were etched with the etchant Keller's reagent (Hydrochloric acid, Hydrofluoric acid, Nitric acid, and distilled water in a ratio of 2:3:5, respectively) for 30 seconds.

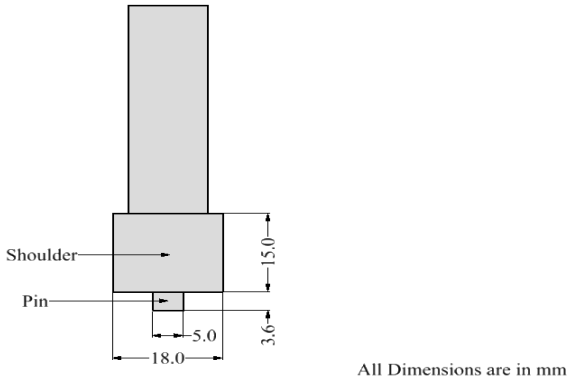

Fig. 1. FSP tool geometry (dimensions in mm)

Table 1. Optical emission spectroscopy analysis of AA2050 alloy

Element	Al	Si	Fe	Cu	Mn	Mg	Zn	Ti	Ag	Li	Others
Weight %	94.3	0.025	0.055	3.52	0.368	0.413	0.034	0.032	0.411	0.76	0.0254

[DOI: 10.22068/ijmse.2670]

Table 2. Friction stir processing trials performed

Trial No	Specimen Code	Tool Rotation Speed (rpm)	Feed rate (mm/min)	No. of Passes
1	A	1000	20	1
2	B	1000	40	1
3	C	1000	60	1
4	D	800	20	1
5	E	800	40	1
6	F	800	60	1
7	G	600	20	1
8	H	600	40	1
9	I	600	60	1
10	J	600	20	2
11	K	600	40	2
12	L	600	60	2

Then the specimen was wiped with cotton laden with acetone. The etched specimen was utilized to observe the macrostructure of the specimens.

The microstructural analysis specimens were prepared and polished as per the methods described in the macrostructure section. To capture the microstructure, the etched specimen was observed under the optical microscope (Make: Carl Zeiss; Model: Axiovert 25).

The microhardness of the specimen was determined using a Vicker's hardness tester (Make: Mitutoyo; Model: MVK-H1). The microhardness was examined at the positions shown in Figure 2 under a load of 300 grams that lasted 10 seconds.

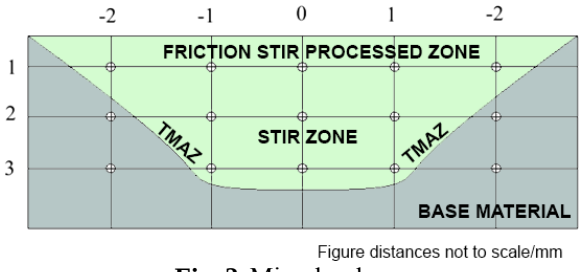

Fig. 2. Microhardness

The tensile test specimens were machined using wire EDM based on the ASTM standards E8/E8M -13a. The sub-size tensile test specimen had a thickness of 5 mm, a width of 6 mm, and a gauge length of 25 mm. The tensile test was conducted at a 0.5 mm/min crosshead speed in a universal testing machine (Make: Tinius Olsen, Model: H25KT).

The macroscopic defect-free specimens were subjected to artificial aging processes. The specimens were heat-treated to T-84 conditions based on ASTM standards. The heat treatment cycle is shown in Figure 3, where heating (a-b) was performed at a heating rate of 5°C/min, followed by aging (b-c) at 160°C for 18 hrs. Then the specimens were furnace-cooled (c-d).

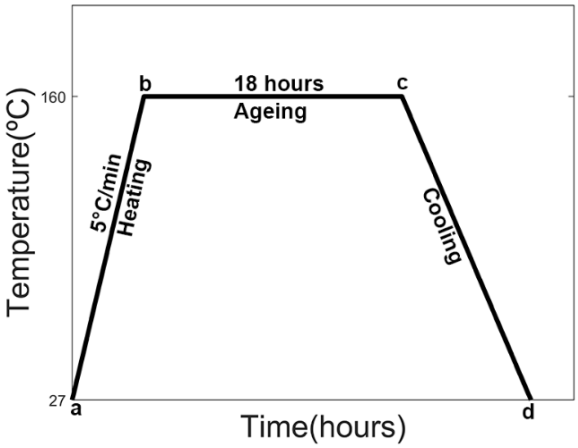

Fig. 3. Heat treatment cycle

The specimens were cut into cuboids of dimension 10 × 10 × 4 mm, and all six faces of the specimen were subjected to standard metallographic specimen preparation. Sodium chloride (NaCl) was mixed with distilled water for pasty consistency. It was then applied on one side of the specimen. The recommended maximum operating temperature for aircraft is 130°C. Hence, 130°C was chosen as the standard temperature for hot salt corrosion. The specimens were loaded inside the digital-temperature controlled furnace and maintained at 130°C for a specific duration. The base material with specimen codes BM 4, BM 2, BM 3, and BM 1 was subject to a hot salt corrosion test for 24, 48, 96, and 168 hours respectively. The test was performed in the base material to find the

[DOI: 10.22068/ijmse.2670]

minimum time required to notice a visible corrosion morphology. As the minimum time to observe corrosion morphology in base material was 168 hours, FSPed specimens were subjected to a hot salt corrosion test in the furnace for 168 hrs.

The surface morphologies of the specimens subjected to tensile and corrosion tests were observed using a field emission scanning electron microscope (Make: Carl Zeiss; Model: Gemini 300). The images were obtained at an electron acceleration voltage of 5 kV and 10 kV at various magnification levels. The elemental composition and map of the corrosion products and corroded regions in the specimens were acquired using an energy-dispersive X-ray spectroscope (Make: Oxford Instruments; Model: Ultima Max) at a high electron tension of 20 kV.

3. RESULTS AND DISCUSSION

3.1. Defect Analysis

Incorporating non-favorable process parameters during FSP trials produced macroscopic and microscopic defects. The defects were primarily related to the material flow and geometrical aspects [20, 21]. The typical defects observed in the FSPed specimens were root flow defects, scalloped surface, and surface lack of fill [22, 23]. The initial FSP trials were performed at 1000 rpm and feed rate of 20 mm/min (specimen A), 40 mm/min (specimen B), and 60 mm/min (specimen C). Specimen A and specimen B were defect-free, whereas specimen C had a surface lack of fill. The defect could be attributed to the high tool rotation speed (1000 rpm) and high feed rate (60 mm/min). The nugget zone in the shape of tool geometry and defects were observed in the specimens after etching. Hence, it was decided to lower the tool rotation speed and maintain the same feed rates.

The subsequent FSP trials were performed at the tool rotation speed of 800 rpm and feed rate of 20 mm/min (specimen D), 40 mm/min (specimen E), and 60 mm/min (specimen F). From the macrostructure analysis, it was observed that specimen E and specimen F had wormholes. Wormholes were the result of the improper flow of material at high speeds. So, the subsequent trials were performed at a still lower tool rotation speed of 600 rpm. The feed rate was varied at 20 mm/min (specimen G), 40 mm/min (specimen H), and 60 mm/min (specimen I). No defects were observed in the macrostructure analysis of specimen G, specimen H, and specimen I. Hence, a second pass (specimen J, specimen K, and specimen L) was performed to analyze the influence of the number of processes on the microstructural evolution of those specimens.

3.2. Heat-Treatment

Based on the macrostructure analysis, the defect-free specimens (specimen G through specimen L) were subjected to heat treatment (T-84 condition). The influence of heat treatment on the microstructure and mechanical properties of the FSPed specimens are discussed in the subsequent sections.

3.3. Microstructure

During FSP, the frictional heating of the FSP tool (tool shoulder and tool pin against the workpiece) plasticized material. The traverse of the FSP tool transferred the plasticized material from the front to the rear position of the tool pin, breaking the grain boundaries. The material flowing around the pin of the tool filled the space behind the tool. Also, the recovery and recrystallization phenomenon resulted in smaller and more refined grains. The typical microstructure indicating the grain refinement and dispersion of intermetallic phases is depicted in Figure 4. The typical microstructure of specimen J, specimen K, and specimen L is shown in Figure 4 (a), Figure 4 (b), and Figure 4 (c), respectively.

The average grain size of specimen G was 25.6 µm, specimen H was 27.2 µm, specimen I was 18.47 µm, specimen J was 17.96 µm, specimen K was 24.45 µm, and specimen L was 23.17 µm. The base material had larger grains, as observed in Figure 4 (c). Conventionally, heat treatment refines the grain size and increases the precipitation of the intermetallic phases in AA2050 alloy [24, 25]. The average grain size of specimen G was 26.23 µm, specimen H was 15.51 µm, specimen I was 21.49 µm, specimen J was 29.36 µm, specimen K was 24.45 µm, and specimen L was 12.96 µm. It is observed that heat treatment has coarsened grains in most of the FSPed specimens. The typical microstructure of specimen K and specimen I are shown in Figures 5 (a) and Figure 5 (b), respectively.

The SEM image and elemental composition of the precipitate in specimen H are shown in Figure 6.

[DOI: 10.22068/ijmse.2670]

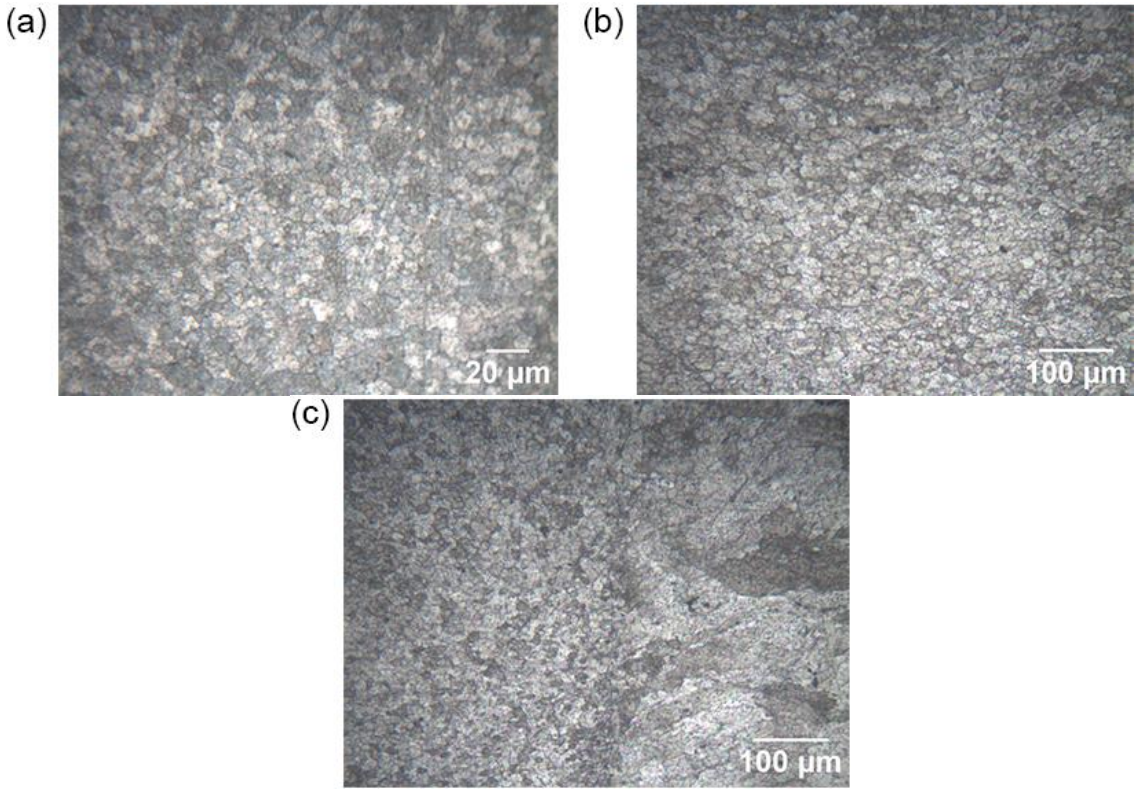

Fig. 4. Microstructure of specimen (a) J at 500× magnification; (b) K at 200× magnification (c) L at 200× magnification

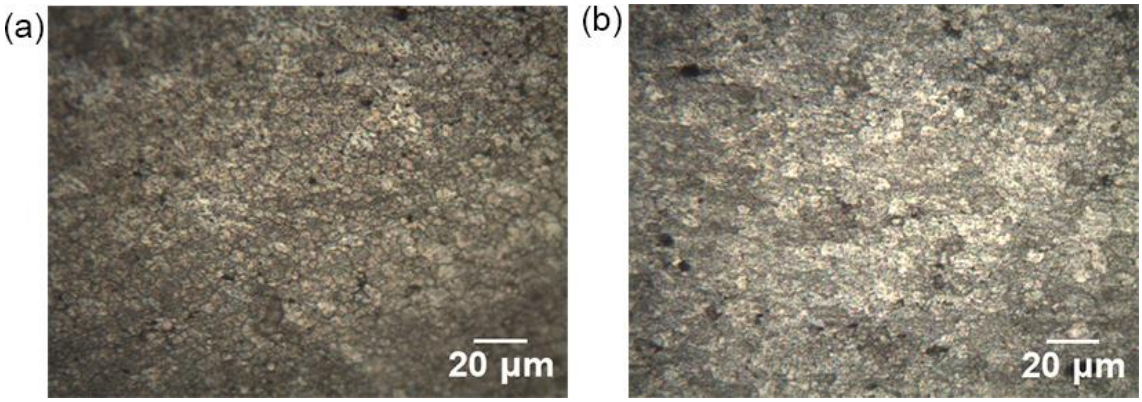

Fig. 5. Microstructure of heat-treated specimen (a) K at 500× magnification; (b) I at 500× magnification

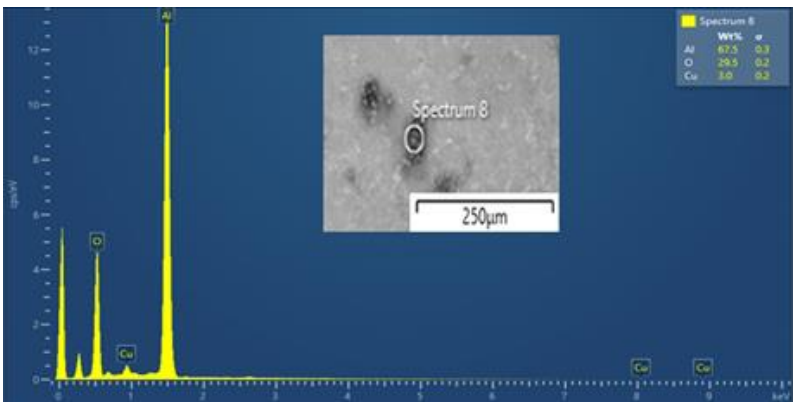

Fig. 6. Microstructure and elemental composition in the mapped region 8

[DOI: 10.22068/ijmse.2670]

The results indicate that the precipitates primarily consisted of Al and Cu. The energy level of the characteristic X-ray of the Li element is lower than the detectable level of the EDS instrument. This may have been attributed to the absence of a Li peak in the elemental composition analysis. The results indicate the presence of primary intermetallic phases of the material T1 (Al_2CuLi), θ' (Al_2Cu), δ' (Al_3Li), and S (Al_2CuMg) were observed in the FSPed specimens [26-28].

3.4. Microhardness

The microhardness is inversely proportional to the grain size of the material. However, not much variation was noticed between the microhardness of FSPed specimens (specimen G through specimen L). All the non-heat-treated FSPed specimens had an average microhardness of 130.86 HV which is greater than that of the non-heat-treated base material (114.28 HV). This is because of the refined microstructure. However, after heat treatment, grains coarsened in the specimens. The coarsening of grains resulted in low microhardness of specimen G (130.8 HV), the specimen I (122.93 HV), specimen J (118.56 HV), and specimen K (130.2 HV). After heat treatment, these specimens had lesser microhardness than the base material (142.48 HV). The Vickers microhardness of the base material (BM) and FSPed specimens before and after heat treatment are shown in Figure 7. Specimen G through specimen L had more hardness in the nugget zone than in other zones.

3.5. Tensile Test

The tensile strength and ductility of the base material and FSPed specimens in heat-treated and non-heat-treated conditions are shown in Figure 8. The tensile strength of the FSPed specimens was lower than the base material. However, the ductility of the material improved after friction stir processing. The base material, specimen G, specimen H, specimen I, specimen J, specimen K, and specimen L had a tensile strength of 402.92 MPa, 352.08 MPa, 363.33 MPa, 391.67 MPa, 333.33 MPa, 361.25 MPa, and 360 MPa respectively. Approximately ~10% reduction was observed in the tensile strength of the FSPed specimens than the base material.

The base material, specimen G, specimen H, specimen I, specimen J, specimen K, and specimen L had an elongation of 28.89%, 30.88%, 33.48%, 37.4%, 34.84%, 39.95%, and 38.92%, respectively. The percentage elongation of most of the non-heat-treated FSPed specimens was higher than the base material. After the tensile test, the fractured region of the base material was observed under the high-resolution scanning electron microscope. The fractography of the base material is shown in Figure 9.

In Figure 9, A indicates cracks, B indicates quasi-cleavage dimples, and C indicates the deformation zone. The plastic deformation zone and quasi-cleavage dimples structures were observed, in line with the previous research work [29]. Some regions with intergranular fracture features indicate a brittle fracture. The fractography indicates that the base material was fractured by a combined ductile (predominantly) and brittle fracture mode. Figure 10 shows the typical fractography of the FSPed specimen (specimen I).

In Figure 10, A indicates cracks, B indicates quasi-cleavage dimples, and C indicates the deformation zone. The specimen had undergone plastic deformation before breaking.

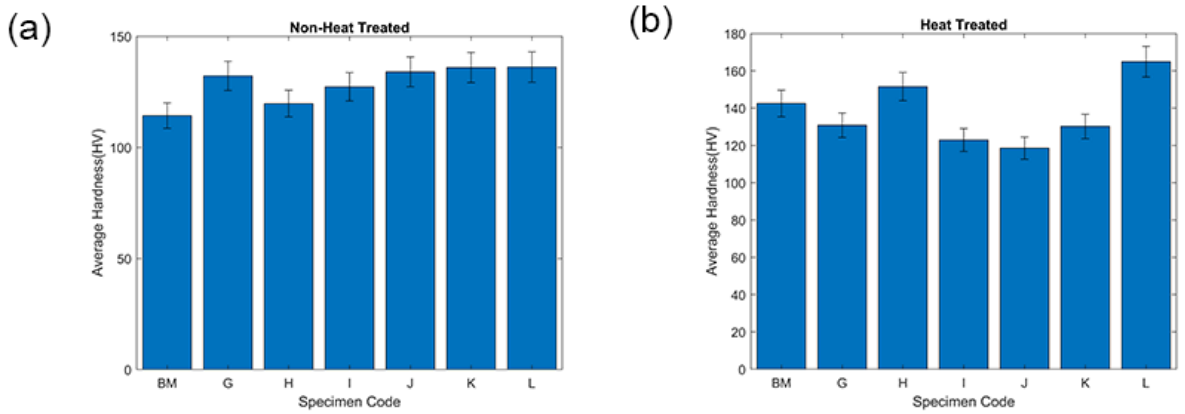

Fig. 7. Microhardness (a) non-heat-treated specimens; (b) heat-treated specimens

[DOI: 10.22068/ijmse.2670]

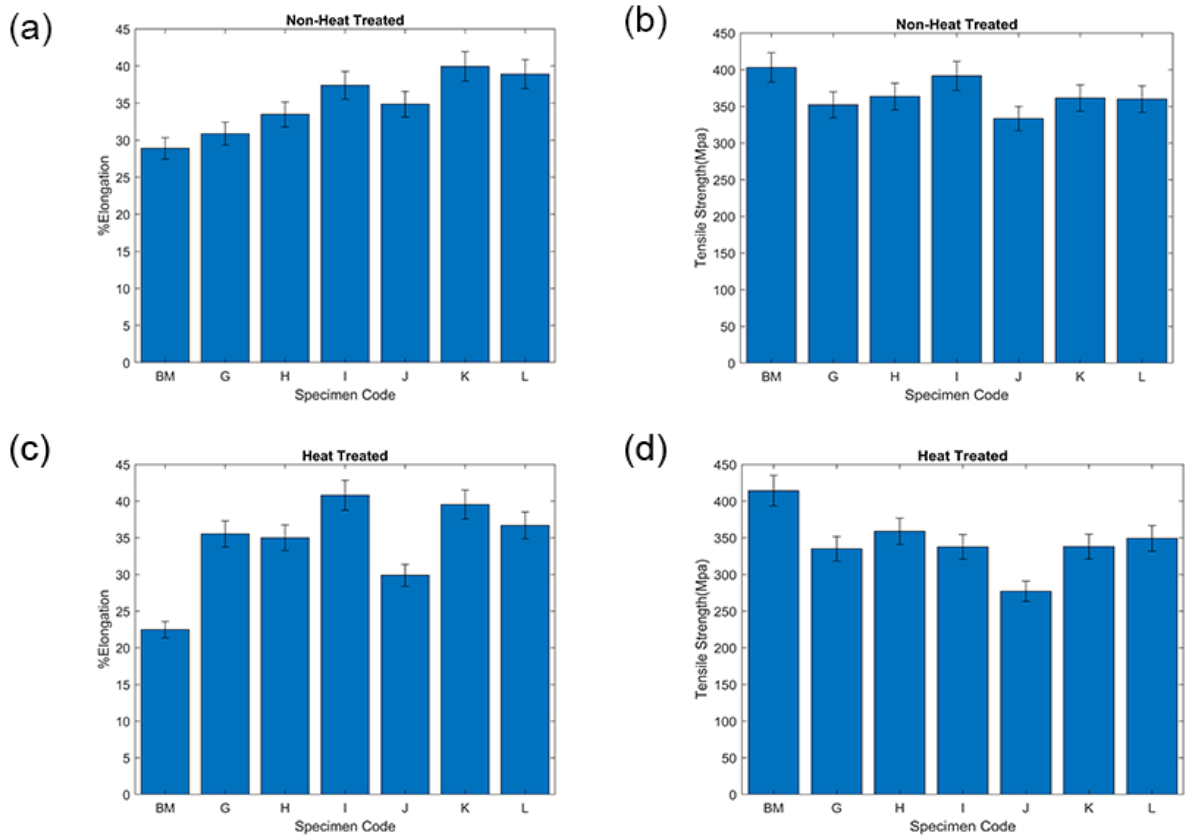

Fig. 8. (a) Non-heat-treated specimens percentage elongation; (b) Non-heat-treated specimens tensile strength; (c) Heat-treated specimens percentage elongation; (d) heat-treated specimens tensile strength

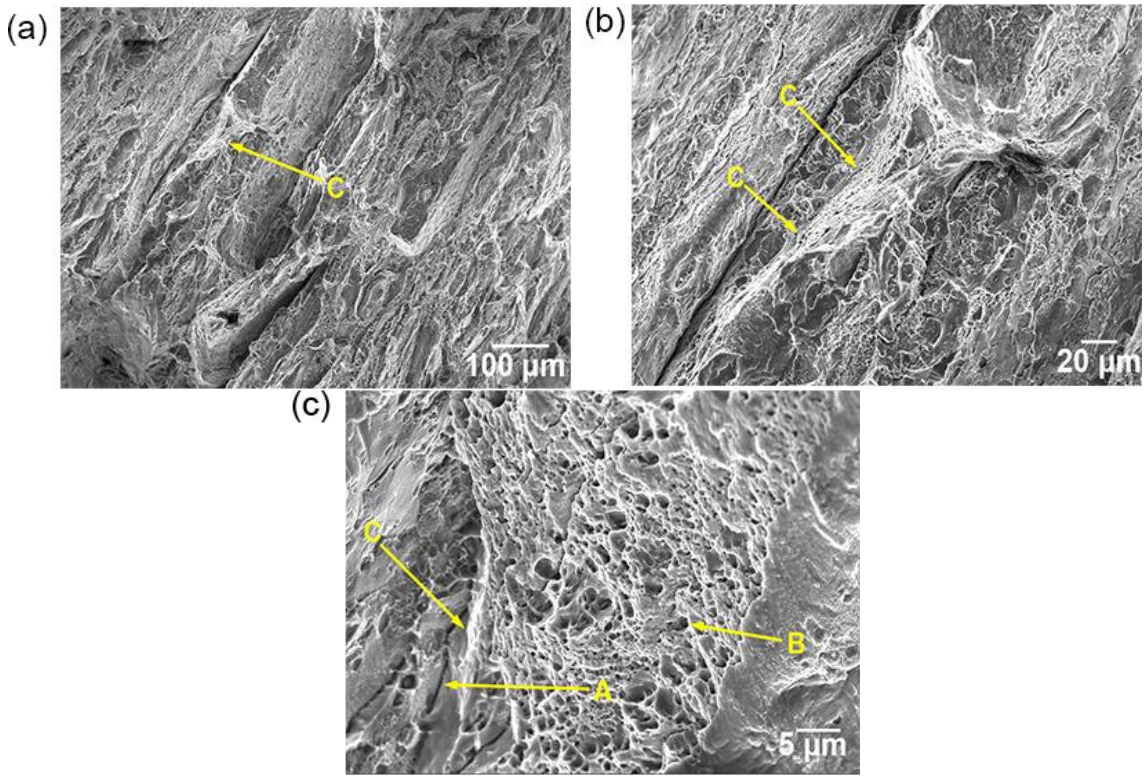

Fig. 9. Fractography of the base material at (a) 125× magnification; (b) 400× magnification; (c) 2000× magnification

[DOI: 10.22068/ijmse.2670]

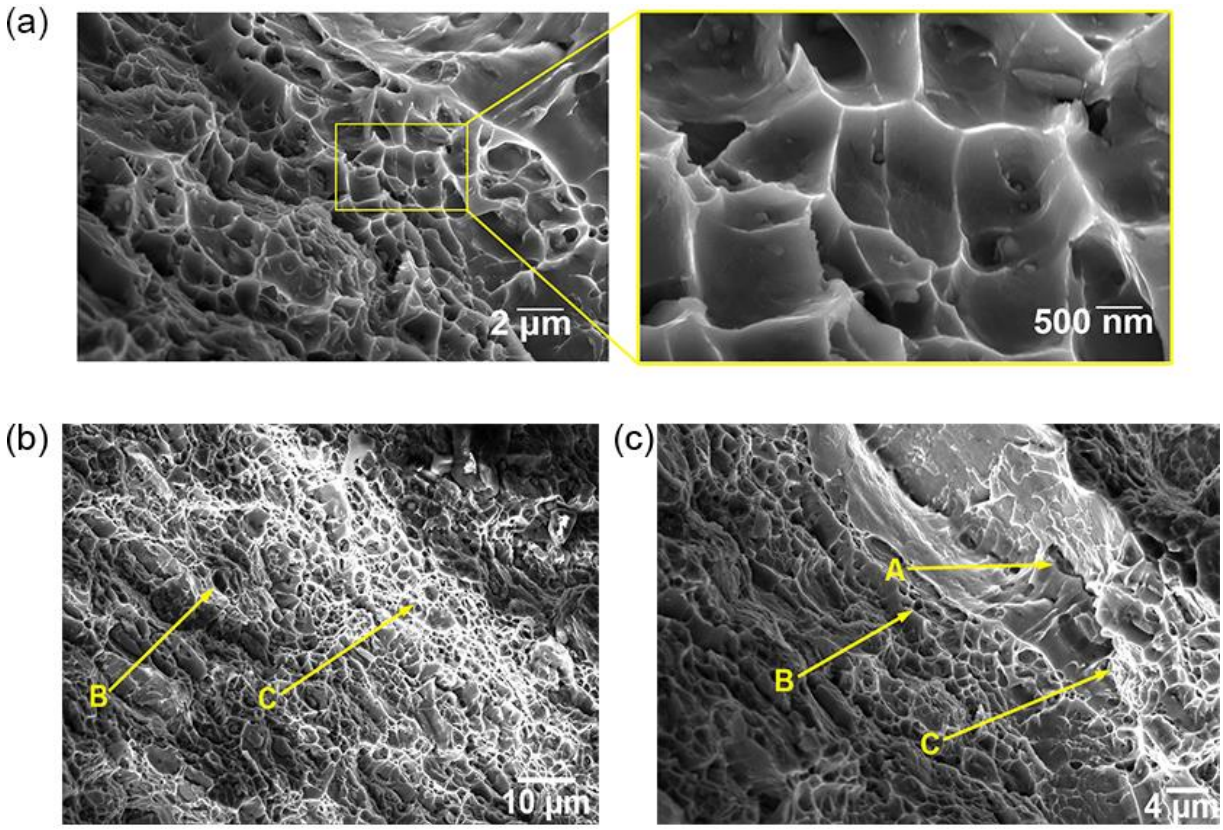

Fig. 10. Fractography of specimen I (a) 5000× magnification; (b) 1250× magnification; (c) 2200× magnification

A magnified image of the fractured region shows quasi-cleavage dimples, which signify the ductile nature of the fracture. The fracture occurred after the complete elongation of the material. This shows that the material had undergone a ductile-dominated fracture.

The average tensile strength of the base material after heat treatment was 414.17 MPa. An increase in the tensile strength of the base material after heat treatment is attributed to the precipitation of intermetallic phases. However, the tensile strength of the FSPed specimens decreased after heat treatment. As described in the microstructure section, an increase in grain size reduced the tensile strength of the FSPed specimens. The average tensile strength of heat-treated specimen G, specimen H, specimen I, specimen J, specimen K, and specimen L was 335 MPa, 358.75 MPa, 337.5 MPa, 277 MPa, 337.92 MPa, and 349.17 MPa, respectively. The percentage elongation of the base material decreased (28.89% to 22.47%) after heat treatment, implying a reduction in ductility. However, the percentage elongation of the FSPed specimens increased after heat treatment. The change in percentage elongation of the specimens before and after heat treatment are specimen G (30.88% to 35.52%), specimen H (33.48% to 35%), specimen I (37.4% to 40.8%), specimen J (34.84% to 29.88%), specimen K (39.95% to 39.52%), specimen L (38.92% to 36.68%) respectively. Figure 11 shows the typical fractographic images of the heat-treated specimen H. In Figure 11, A indicates the zone of deformation. More plastic deformation of the material is evident in the heat-treated specimen, as shown in Figure 11. Also, quasi-cleavage dimples were observed on the fractured surface, as shown in Figure 11 (a). Intergranular fracture features in the fractured zone are shown in Figure 11 (b) and Figure 11 (c). It is inferred that the specimen was fractured by combined ductile (predominantly) and brittle fractures.

3.6. Hot Salt Corrosion

The non-heat-treated FSPed specimens were subjected to a hot salt corrosion test as per the methodology described in the methodology section. The mass loss per unit area of the base material and the FSPed specimens subjected to corrosion tests are shown in Figure 12 (a) and

[DOI: 10.22068/ijmse.2670]

figure F2 (b), respectively. The mass loss per unit area after 24 hours (BM-4), 48 hours (BM-2), 96 hours (BM-3), and 168 hours (BM-1) were 0.0698 mg/cm^2, 0.1388 mg/cm^2, 0.3311 mg/cm^2 and 0.6342 mg/cm^2 respectively. As significant corrosion occurred at 168 hours, all the FSPed specimens were subjected to a corrosion test for 168 hours. Specimen J had a mass loss per unit area of 0.8183 mg/cm^2, the highest among all the FSPed specimens. The mass loss per unit area of Specimen G was 0.4546 mg/cm^2, which was closer to the mass loss per unit area of the base material (0.6342 mg/cm^2). The mass loss per unit area of specimen H, specimen K, and specimen L were 0.0770 mg/cm^2, 0.0667 mg/cm^2, and 0.0699 mg/cm^2, respectively. Those specimens had a lower mass loss per unit area than the base material. The specimen I had a minor mass loss per unit area of 0.0606 mg/cm^2. The corrosion test results show that FSP improves the hot corrosion resistance of AA2050 alloy. The surface morphology and elemental composition of the specimens subjected to corrosion test are shown below:

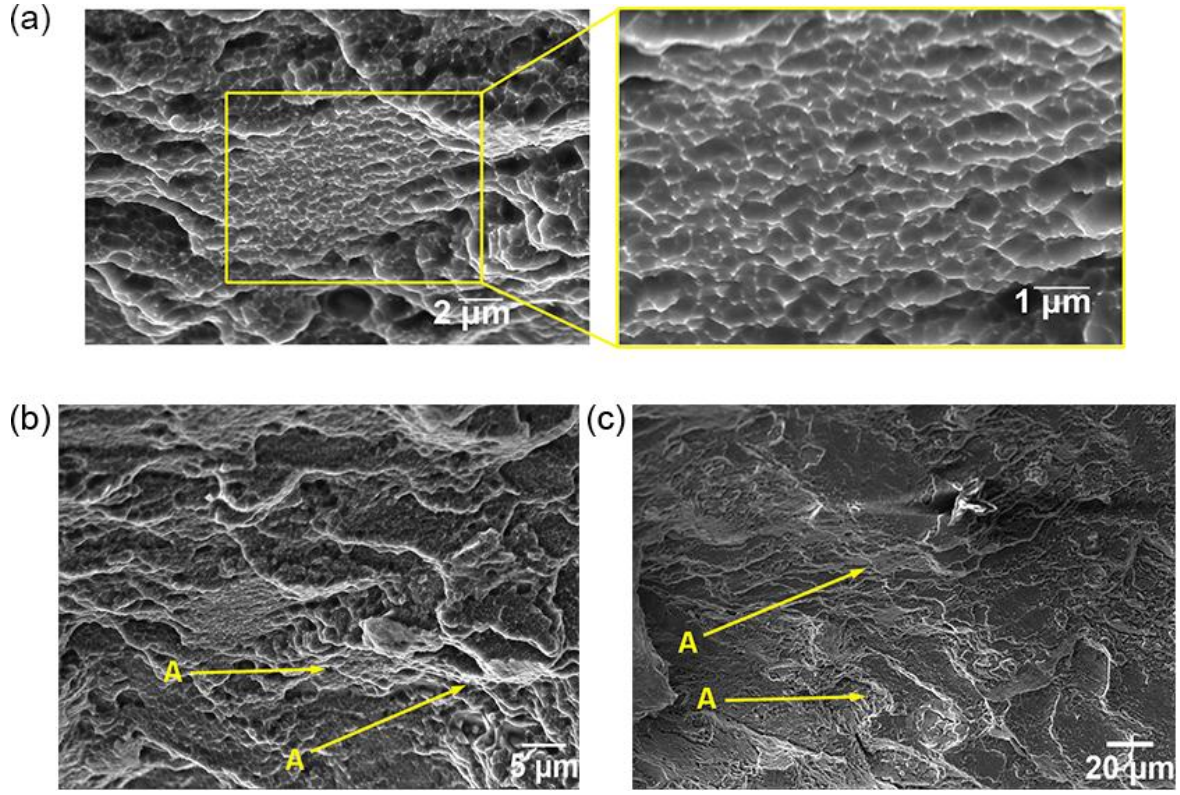

Fig. 11. Fractography of heat-treated specimen H at (a) 6000× magnification; (b) 2000× magnification; (c) 500× magnification

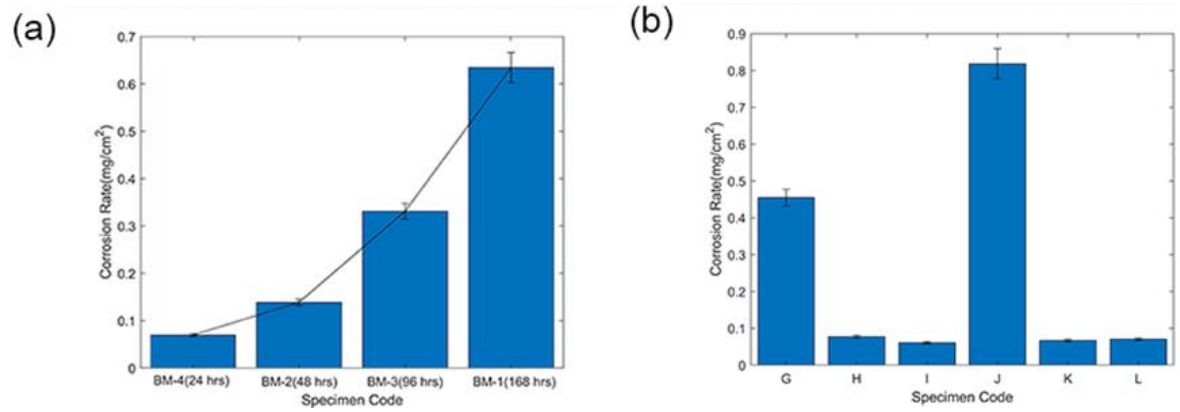

Fig. 12. Hot-salt corrosion test - mass loss per unit area (a) Base material; (b) FSPed specimens (after 168 hours)

[DOI: 10.22068/ijmse.2670]

Figure 13 shows the surface morphology of the top surface of the base material after the hot corrosion test. In Figure 13, A indicates a corroded surface, and B indicates a corrosion product. Figure 13 (a) shows a rough patch on the material surface, which is the corrosion product. Figure 13 (b) shows the magnified view of the corroded region. The black spots in Figure 13 indicate the formation of pits in the course of corrosion. The side-view of specimen G is shown in Figure 14. In Figure 14, A indicates a corroded surface, B indicates a corrosion product, and C indicates sub-surface cracks. Figure 14 (a) shows the propagation of corrosion from the top surface of specimen G. The corrosion had propagated to a depth of 148.5 µm from the top surface of specimen G after 168 hours. The cracks formed in the course of hot salt corrosion are depicted in Figure 14 (b). The rough patch is the corrosion product, as shown in Figure 14 (c). The elemental map of corroded specimen K is shown in Figure 15. Figure 15 (a) shows the chosen region for the elemental map, and Figure 15 (b) shows the consolidated elemental map of the chosen region.

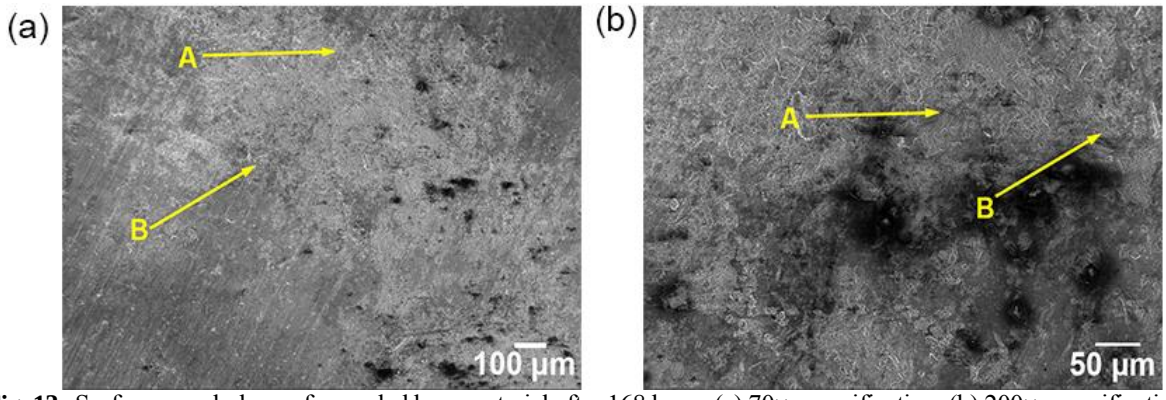

Fig. 13. Surface morphology of corroded base material after 168 hours (a) 70× magnification; (b) 200× magnification

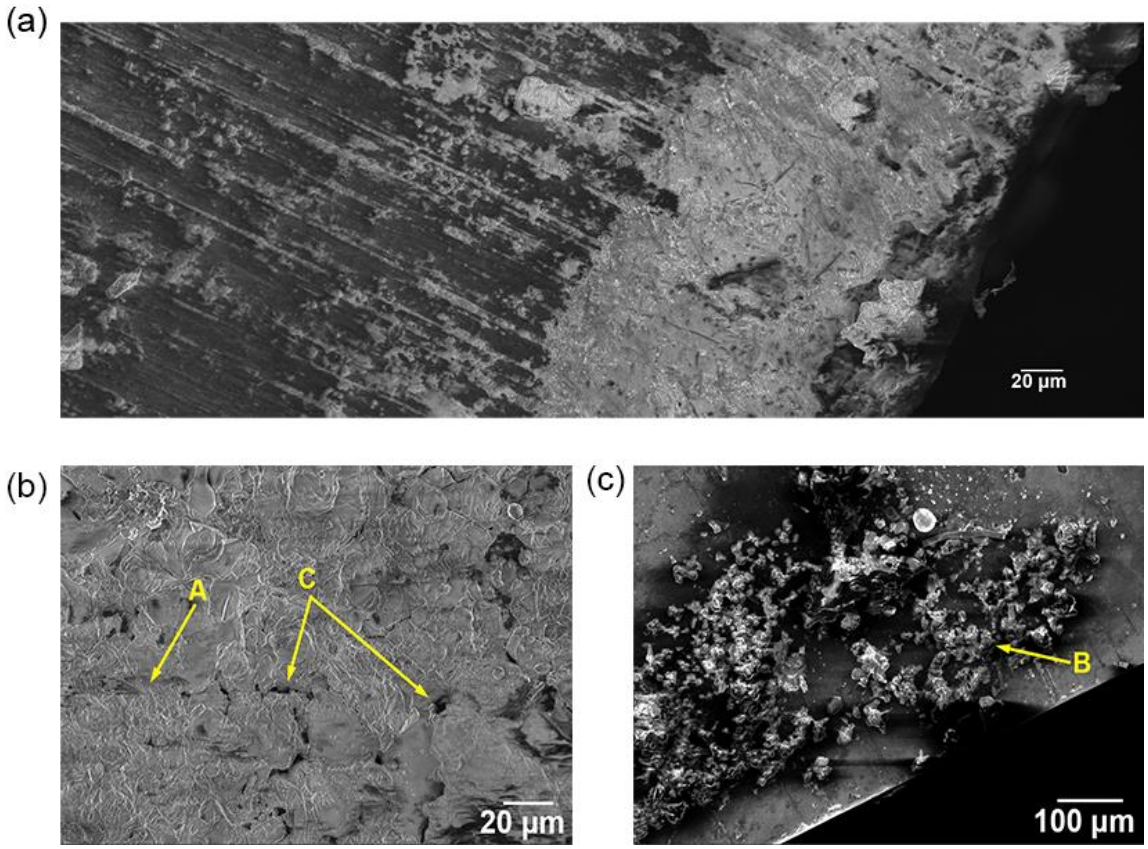

Fig. 14. Surface morphology of specimen G (a) 65× magnification (b) 150× magnification (c) 400× magnification

[DOI: 10.22068/ijmse.2670]

The elemental map Al, O, Cu, Na, Mg, Cl, and Si of the chosen region is shown in Figure 15 (c), Figure 15 (d), Figure 15 (e), Figure 15 (f), Figure 15 (g), Figure 15 (h) and Figure 15 (i) respectively.

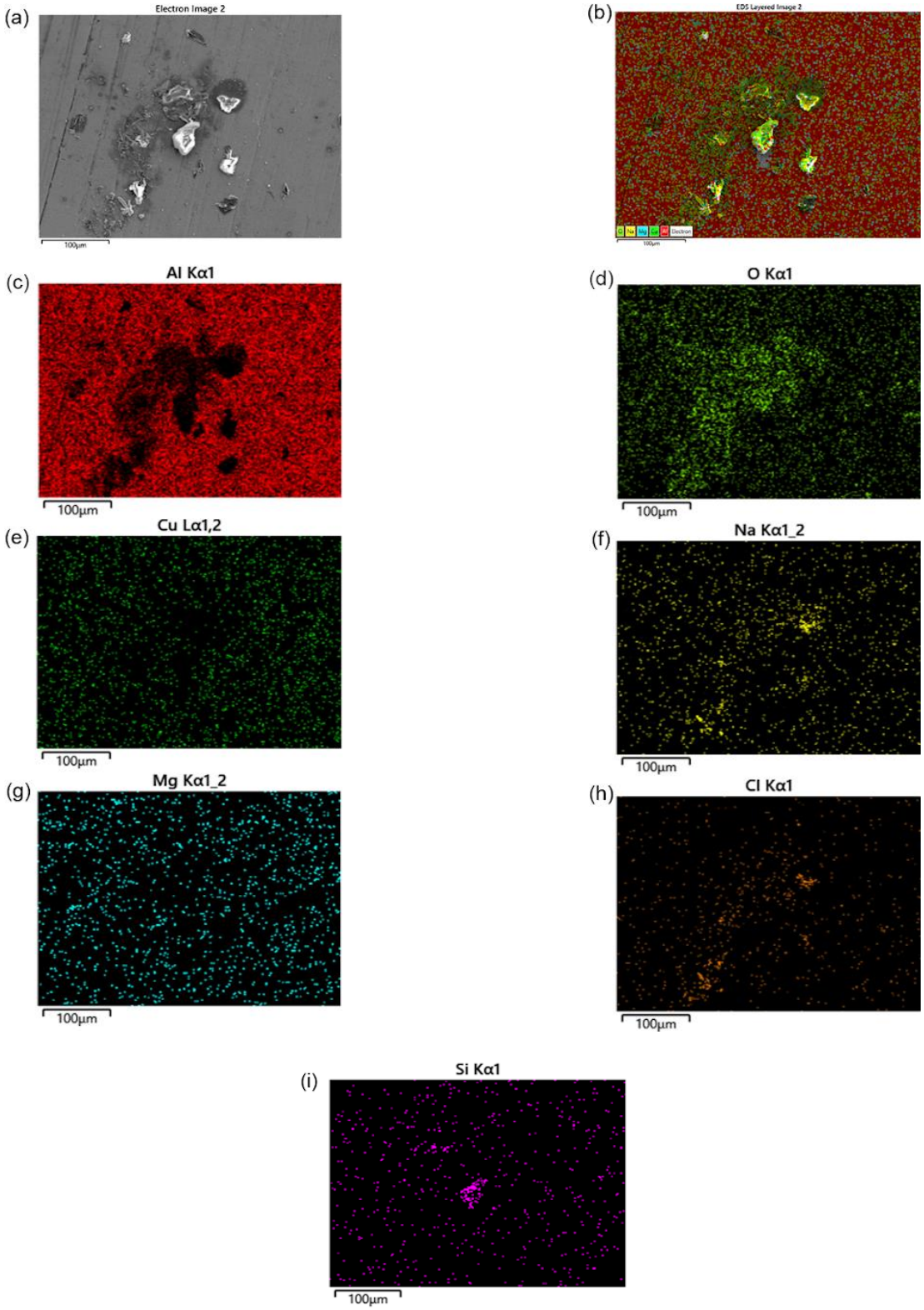

Fig. 15. Elemental map of the corroded specimen (a) Surface morphology; (b) Consolidated elemental map; (c) Elemental map of Aluminium; (d) Elemental map of oxygen; (e) Elemental map of Copper; (f) Elemental map of Sodium; (g) Elemental map of Magnesium; (h) Elemental map of Chlorine; (i) Elemental map of Silicon

[DOI: 10.22068/ijmse.2670]

The significant proportion of Al and Cu in the elemental map is attributed to the alloy composition. The presence of traces of impurities in the base material matrix resulted in the minor proportions of Si and Mg in the elemental map. The presence of O indicates the formation of an oxide layer on the surface of specimen K during the hot-corrosion test. Na and Cl were also detected in this region, as evidenced by the elemental map of Na and Cl. That could be from the residual salt on the surface. Besides, the formation of $AlCl_3$ could have been attributed to the elemental map of Cl. The hot corrosion test indicates that oxidative corrosion is predominant in Al-Cu-Li at high temperatures.

θ-Al_2O_3, a metastable alumina phase, made up the original phase composition of the oxide scale. However, when the oxidation duration increased, θ-Al_2O_3 changed into α-Al_2O_3. The counter diffusion of aluminum and oxygen promoted the growth of alumina scales. The Al and O ions in the scale were most likely transported by a grain boundary diffusion. The substrate was well-adhered to the alumina scale. Also, oxide layer formation was driven by atomic diffusion and surface energy reduction.

The surface and grain boundary segregation of alloying elements enhances the chemical heterogeneity and causes corrosion issues. Hence, elemental segregation is not desired in applications for aircraft construction. The segregation of Cu along grain boundaries would result in intergranular corrosion, stress corrosion cracking, and hydrogen embrittlement. Also, surface segregation of Li, a reactive element, might alter the surface characteristics and cause corrosion issues. The alloying elements were homogeneously distributed in the surface oxide in the friction stir processed specimens. In the case of Cu, no localized distribution in the oxide part over the grain boundaries of the Al alloy substrate was observed. Hence, the absence of surface segregation and grain boundary segregation of alloying elements promoted corrosion resistance of the friction stir processed specimens.

4. CONCLUSIONS

Friction stir processing of AA2050 was performed by varying the friction stir processing parameters. The microstructure, microhardness, tensile strength, and mass loss per unit area of defect-free specimens were analyzed. Also, the influence of artificial aging on the properties of the friction stir processed specimen was investigated. The results established the following:

- More refined grains than base material were observed in the friction stir processed zone.
- The increased FSP passes improved the microhardness and ductility of the friction stir processed specimens. However, the tensile strength of the double-pass FSPed specimen decreased with respect to the base material counterparts.
- The heat treatment has a negligible effect on the microhardness of the friction stir processed specimens. The tensile strength of FSPed specimens decreased with heat treatment. However, the percentage of the elongation in the specimens was higher than in the base material.
- Most friction stir processed specimens (single pass and double pass) had less mass loss per unit area than the base material.
- Among the tested specimens, specimen I, processed at 600 rpm with a 60 mm/min feed rate and a single pass, had similar tensile strength, substantially higher microhardness, and % elongation than the base material. Also, the mass loss per unit area of the specimen was 90% lesser than the base material. Hence, the optimum FSP process parameters for maximizing the strength, ductility, hardness, and corrosion resistance of AA2050 alloy are concluded as a tool rotation speed of 600 rpm, feed rate of 60 mm/min, and single-pass.

DECLARATIONS

Funding

The authors and co-authors did not receive a specific grant from any funding agency in the public, commercial, or not-for-profit sectors to carry out the research.

Conflicts of interest/Competing interests

The authors declare that there is no conflict of interest or competing interests for the research work.

REFERENCES

[1]. H. He, Y. Yi, J. Cui, and S. Huang, "Hot

[DOI: 10.22068/ijmse.2670]

deformation characteristics and processing parameter optimization of 2219 Al alloy using constitutive equation and processing map," Vacuum, 2019, 160, 293-302.
[2]. J. Jiang, T. Yuan, W. Zhang, A. Ma, D. Song, and Y. Wu, "Effect of equal-channel angular pressing and post-aging on impact toughness of Al-Li alloys," Mater. Sci. Eng., A, 2018, 733, 385-392.
[3]. R. Kapil, R. Jayaganthan, S. Gairola, and R. Verma, "Improvement of fracture toughness of ultra fine grained Al–Li 8090 alloy processed through multi axial forging," Mater. Res. Express, 2019, 6, 8, 085064.
[4]. J. Han, Z. Zhu, H. Li, and C. Gao, "Microstructural evolution, mechanical property and thermal stability of Al–Li 2198-T8 alloy processed by high pressure torsion," Mater. Sci. Eng., A, 2016, 651, 435-441.
[5]. J. Zhang, Z. Jiang, F. Xu, and M. Chen, "Effects of Pre-Stretching on Creep Behavior, Mechanical Property and Microstructure in Creep Aging of Al-Cu-Li Alloy," Materials, 2019, 12, 3, 333.
[6]. M. Attallah and H. Salem, "Influence of process parameters on superplasticity of friction stir processed nugget in high strength Al–Cu–Li alloy," Mater. Sci. Technol., 2004, 20, 11, 1370-1376.
[7]. K. Surekha, B. Murty, and K. P. Rao, "Microstructural characterization and corrosion behavior of multipass friction stir processed AA2219 aluminium alloy," Surf. Coat. Technol., 2008, 202, 17, 4057-4068.
[8]. Y. Lin, C. Lu, C. Wei, and Z. Zheng, "Effect of aging treatment on microstructures, tensile properties and intergranular corrosion behavior of Al–Cu–Li alloy," Mater. Charact, 2018, 141, 163-168.
[9]. P. Wu, Y. Deng, S. Fan, H. Ji, and X. Zhang, "A study on dissimilar friction stir welded between the Al–Li–Cu and the Al–Zn–Mg–Cu alloys," Materials, 2018, 11, 7, 1132.
[10]. S. Mehrez, M. Paidar, K. Cooke, R. V. Vignesh, O. O. Ojo, and B. Babaei, "A comparative study on weld characteristics of AA5083-H112 to AA6061-T6 sheets produced by MFSC and FSSW processes," Vacuum, 2021, 190, 110298.
[11]. S. Liu et al., "Probe-less friction stir spot processing (PFSSP) of AA5754/AA5083 joint by adding the B4C ceramics: Effect of shoulder features on mechanical properties and tribological behavior," Vacuum, 2023, 207, 111542.
[12]. Ramalingam, V.V., Ramasamy, P. and Datta, M. (2019), "Microstructure, hardness and corrosion behaviour of friction-stir processed AA5083", Anti-Corrosion Methods and Materials, Vol. 66 No. 6, pp. 791-801. https://doi.org/10.1108/ACMM-07-2017-1816.
[13]. M. Abijith, A. R. Nair, M. Aadharsh, R. V. Vignesh, R. Padmanaban, and M. Arivarasu, "Investigations on the Mechanical, Wear and Corrosion Properties of Cold Metal Transfer Welded and Friction Stir Welded Aluminium Alloy AA2219," Jordan Journal of Mechanical & Industrial Engineering, 2018, 12, 4,
[14]. S. P. Dwivedi, "Effect of process parameters on tensile strength of friction stir welding A356/C355 aluminium alloys joint," J. Mech. Sci. Technol., 2014, 28, 1, 285-291.
[15]. X. Zheng, P. Luo, Z. Chu, J. Xu, and F. Wang, "Plastic flow behavior and microstructure characteristics of light-weight 2060 Al-Li alloy," Mater. Sci. Eng., A, 2018, 736, 465-471.
[16]. M. Barati, M. Abbasi, and M. Abedini, "The effects of friction stir processing and friction stir vibration processing on mechanical, wear and corrosion characteristics of Al6061/SiO2 surface composite," J. Manuf. Processes, 2019, 45, 491-497.
[17]. B. Cai, Z. Zheng, D. He, S.-C. Li, and H. Li, "Friction stir weld of 2060 Al–Cu–Li alloy: Microstructure and mechanical properties," J. Alloys Compd., 2015, 649, 19-27.
[18]. L. Khokhlatova, N. Kolobnev, and V. Ovchinnikov, "Properties and structure of friction stir welded joints in 1424 and V-1461 (Al–Li) alloys," Weld. Int., 2018, 32, 1, 62-66.
[19]. Alloys, Wrought Aluminum. "International Alloy Designations and Chemical

[DOI: 10.22068/ijmse.2670]

Composition Limits for Wrought Aluminum and." (2015). Link: https://www.aluminum.org/sites/default/files/2021-10/Teal%20Sheet.pdf.

[20]. R. V. Vignesh, R. Padmanaban, and M. Govindaraju, "Investigations on the surface topography, corrosion behavior, and biocompatibility of friction stir processed magnesium alloy AZ91D," Surf. Topogr. Metrol. Prop., 2019, 7, 2, 025020.

[21]. R. Vaira Vignesh, R. Padmanaban, M. Govindaraju, and G. Suganya Priyadharshini, "Investigations on the corrosion behaviour and biocompatibility of magnesium alloy surface composites AZ91D-ZrO_2 fabricated by friction stir processing," Trans. IMF, 2019, 97, 5, 261-270.

[22]. R. Padmanaban, V. Balusamy, and R. Vaira Vignesh, "Effect of friction stir welding process parameters on the tensile strength of dissimilar aluminum alloy AA2024-T3 and AA7075-T6 joints," Materialwiss. Werkstofftech., 2020, 51, 1, 17-27.

[23]. M. Govindaraju, R. V. Vignesh, and R. Padmanaban, "Effect of heat treatment on the microstructure and mechanical properties of the friction stir processed AZ91D magnesium alloy," Met. Sci. Heat Treat., 2019, 61, 5, 311-317.

[24]. N. Nayan, S. N. Murty, S. Chhangani, A. Prakash, M. Prasad, and I. Samajdar, "Effect of temperature and strain rate on hot deformation behavior and microstructure of Al-Cu-Li alloy," J. Alloys Compd., 2017, 723, 548-558.

[25]. A. Bois-Brochu, C. Blais, F. A. T. Goma, and D. Larouche, "Modelling of anisotropy for Al-Li 2099 T83 extrusions and effect of precipitate density," Mater. Sci. Eng., A, 2016, 673, 581-586.

[26]. B. Rodgers and P. Prangnell, "Quantification of the influence of increased pre-stretching on microstructure-strength relationships in the Al–Cu–Li alloy AA2195," Acta Mater., 2016, 108, 55-67.

[27]. M. Munoz-Morris and D. G. Morris, "Severe plastic deformation processing of Al–Cu–Li alloy for enhancing strength while maintaining ductility," Scr. Mater., 2010, 63, 3, 304-307.

[28]. H. Gao, T. Weng, J. Liu, C. Li, Z. Li, and L. Wang, "Hot stamping of an Al-Li alloy: a feasibility study," Manuf. Rev., 2016, 3, 9.

[29]. A. Abd El-Aty, Y. Xu, S. Zhang, Y. Ma, and D. Chen, "Experimental investigation of tensile properties and anisotropy of 1420, 8090 and 2060 Al-Li alloys sheet undergoing different strain rates and fibre orientation: a comparative study," Procedia Eng., 2017, 207, 13-18.

[DOI: 10.22068/ijmse.2670]